

BEAMLET LASER DIAGNOSTICS

S. C. Burkhardt

W. C. Behrendt

I. Smith

Introduction

Beamlet is instrumented extensively to monitor the performance of the overall laser system and many of its subsystems. Beam diagnostics, installed in key locations, are used to fully characterize the beam during its propagation through the multipass cavity and the laser's output section (Fig. 1). This article describes the diagnostics stations located on Beamlet and discusses the design, calibration, and performance of the Beamlet calorimeters. We used Nova's diagnostics packages to develop the Beamlet design to determine beam energy, spatial profile, temporal profile, and other beam parameters.^{1,2} Technologic improvements within the last several years in controls, charge-coupled device (CCD) cameras, and fast oscilloscopes have allowed us to obtain more accurate measurements on the Beamlet laser system. We briefly cover some of these techniques, including a description of our LabVIEW³ based data acquisition system.

Diagnostics Systems

The first diagnostics station in the main laser is at the east end of the cavity where the beam is sampled after the first pass through the amplifier (Fig. 1). The cavity mirrors are designed to leak approximately 0.5% of the incident $1.053\text{-}\mu\text{m}$ (1ω) light, which is down-collimated to a near-field camera, an energy diode, a temporal pulse-shape diode, and an absorbing glass calorimeter. The beam is diagnosed in a similar manner at the west end of the cavity following the second pass through the laser. The third and fourth passes are also sampled and diagnosed to a limited extent, since the imaging and energy diagnostics can only view one pass for any particular shot. In addition, only the depolarized portion of the fourth pass is transmitted through the polarizer to the west cavity diagnostics.

At the output of the 1ω section of the laser, the beam is again sampled using the reflection off an uncoated

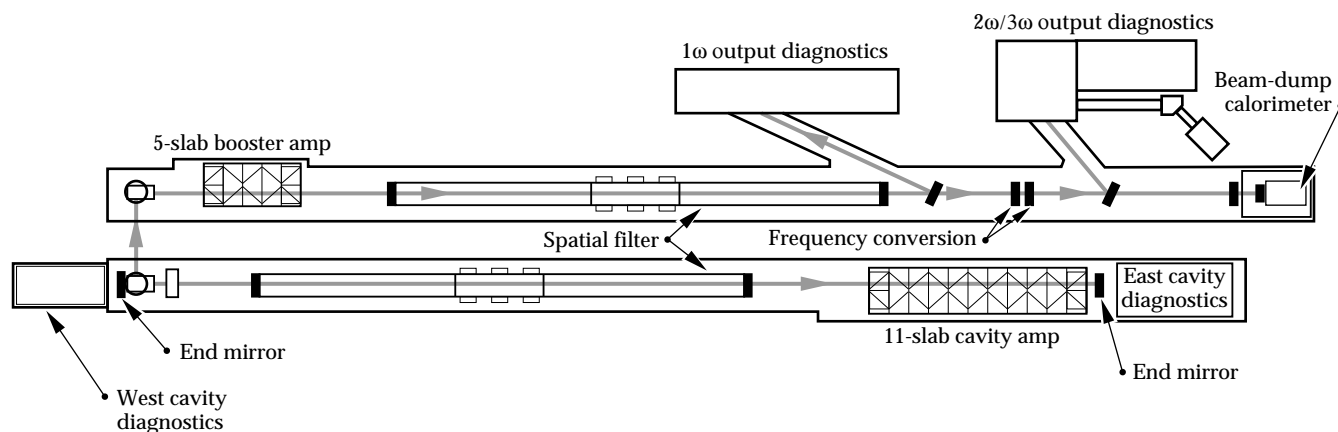


FIGURE 1. View of the Beamlet laser and the diagnostics systems. Dedicated diagnostics are located at both ends of the main cavity and at the output section prior to, and after, the frequency conversion crystals. An instrumented beam-dump calorimeter absorbs all of the remaining beam. (70-50-0395-0662pb01)

fused-silica beamsplitter (Fig. 1). This 1ω output package contains an extensive suite of diagnostics including energy, temporal pulse shape (diode and streak camera), low- and high-resolution near- and far-field imaging, phase front (Hartmann array and a radial-shear interferometer), and beam bandwidth (Fabry-Perot). Another large set of diagnostics are present in the $2\omega/3\omega$ diagnostics station that follows the frequency conversion section. This diagnostics package also includes a beam energy balance system that measures the absolute energy in each of the primary (1ω), doubled (2ω), and tripled (3ω) beams. The last diagnostics station consists solely of a single, large-aperture, 74-cm absorbing glass calorimeter that quantifies the combined output beam energy (minus, of course, the small amount of energy that is deflected to the previous diagnostics systems). This calorimeter also serves as a “beam dump.”

Cavity Diagnostics

Cavity diagnostics are located at both ends of the main amplifier cavity, with the diagnostic transport shown in Fig. 2 for the east cavity diagnostics. For

diagnostic purposes, the cavity mirrors leak a nominal 0.4–1% of the incident beam and the transmitted beam passes through the uncoated backside and the antireflective (AR) coated 7.6-m focusing lens. The converging beam is folded twice by the upper and lower turning mirrors; attenuated by one or two 99.3% mirrors (Fig. 3); and split to the far-field camera, the near-field camera, and to an integrating sphere/photo-diode energy diagnostic. The rejected beam from the first attenuator mirror is directed to a calorimeter and a temporal pulse-shape vacuum photodiode diagnostic. The cameras and integrating sphere are discussed here; the calorimeter and temporal diagnostics are discussed in subsequent sections. Figure 2 shows the east cavity diagnostics, including extensive baffling. This baffling prevents the intense off-axis flashlamp light, transmitted through the cavity mirror, from reaching the diagnostics.

The near-field camera (a Cohu 6400 series) images the cavity mirror directly onto the CCD camera through an attenuating protective window mounted on the camera's face. To achieve the right intensity, the beam is transmitted through filter-wheel-mounted neutral-density filters. These filters consist of AR-coated

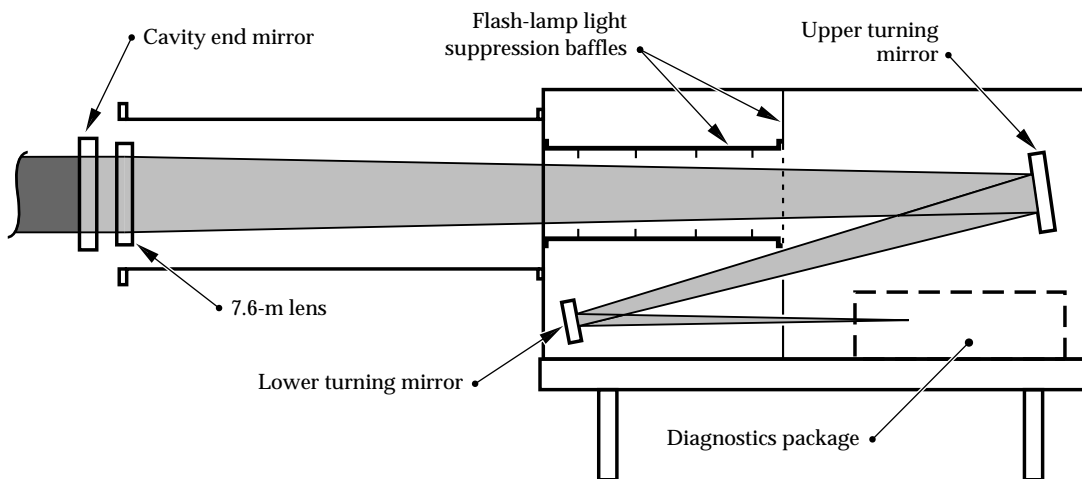


FIGURE 2. Side view of the cavity diagnostic beam transport optics. The 0.5% leakage through the cavity end mirror is focused and folded down to the diagnostic package. The east and west end diagnostic transport optics are identical, but the east diagnostics are substantially baffled to prevent the light of the adjacent cavity amplifier flash lamps from saturating the diagnostics. (70-50-0494-1667pb01)

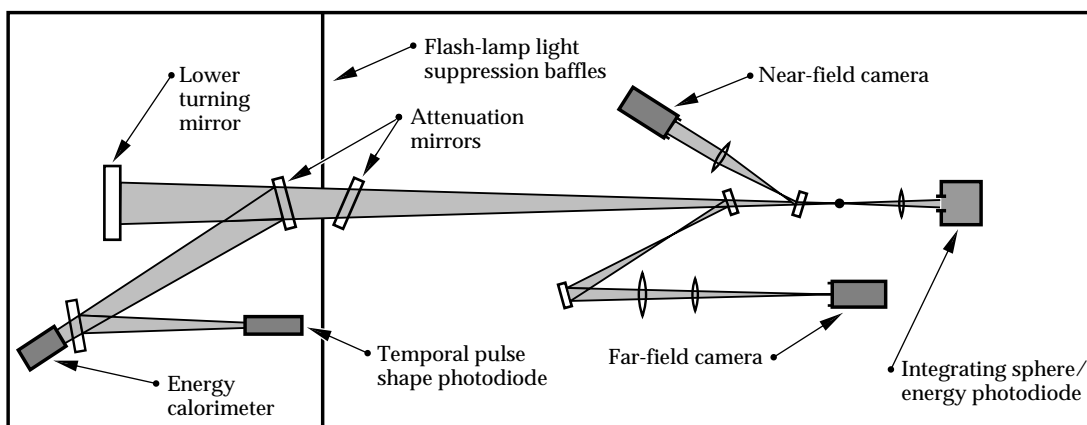


FIGURE 3. Top view showing the east cavity diagnostics. Attenuating filters, beam blocks, and pinholes strip off ghost images, select the desired cavity pass, and set the energy levels to each diagnostic. (70-50-0494-1666pb01)

31-mm-diam glass (NG-1, NG-3, NG-4, NG-5, NG-9, and NG-11). The image is viewed on the alignment display through the Beamlet video switching system for beam centering, with the attenuator mirrors replaced by identical AR-coated blanks. To capture the near-field image during a shot, the attenuator mirrors and filters are set to calculated values, and the 16-channel framegrabbing system is triggered to capture the image field at shot time. The near-field camera is quite useful for centering operations and for shots; however, automation of the attenuator mirror insertion is needed as Beamlet's shot rate increases. The camera images either pass 1 or pass 3 (pass 2 or pass 4 for the west cavity diagnostics) with automated selection between the passes. A stepper-motor-mounted pinhole array at the focus selects pass 1, pass 3, or both passes simultaneously, and strips off the unwanted image from the uncoated back surface of the cavity mirror.

The far-field camera has a complicated design to perform both the diagnostic and pointing functions. The compromised design limited its performance in diagnostic mode, and the pointing function was superseded by a telescope mounted at the cavity pinhole plane. The camera had two fields of view of the cavity spatial filter pinhole plane. The first field (a 4×4 cm image) viewed all four cavity spatial filter pinholes simultaneously for pointing purposes. The other field (a higher resolution 8×8 mm image) required manual replacement of several lenses, and viewed one pinhole at a time. To achieve the wide field of view required a fast lens mounted directly in front of the camera imaging surface. To do this, we glued the lens onto a faceplate ring that replaced the CCD protective cover. In addition, several oversized lenses were required to perform high-quality off-axis far-field imaging. We designed the far-field camera to perform Beamlet pointing in the wide field of view mode, an operation now routinely performed by the Questar telescope. For a time, the camera was used in shot mode, but the angular resolution was too small to be of much use. Thus, the camera was removed as Beamlet activation proceeded to, and beyond, the four-pass experiments.

During the activation stage, the integrating sphere energy diagnostic proved to be exceedingly useful and was instrumental in determining the plasma electrode Pockels cell performance in the west cavity diagnostics. The system consists of a Labsphere 4-in.-spectralon integrating sphere with an EG&G FND-100 Si photodiode reverse biased to 40 V and recorded by a Tektronix TDS-320 digitizing oscilloscope. The bias voltage is

coupled in by a Picosecond Pulse Lab bias tee, and the signal is terminated in 50Ω at the oscilloscope. During initial activation, especially continuous-wave (cw) tests, a slower, more sensitive PIN-8 diode replaced the FND-100 photodiode. The PIN-8 diode was battery biased with the bias tee removed to transmit the 350- μ s gain test signal, and the signal was recorded by the TDS-320 in high-impedance mode. In later, more routine, system operations, the integrating sphere signals were recorded but were used largely in a qualitative sense. Software was developed to calculate the charge delivered by the photodiode from the recorded voltage waveform and to infer the energy from the calibrated sensitivity and system transmission. However, with our extensive use of inexpensive and very accurate calorimeters, the integrating sphere energy diagnostic was used only as a relative comparison between the passes and as a post-mortem for shots which did not perform as expected.

1 ω Output Diagnostics

A portion of the fully amplified Beamlet beam is sampled by a 61-cm beamsplitter and relay imaged to the 1 ω diagnostic station (Fig. 4). The beam sample is approximately 3% of the main beam from the 12° angle of incidence "P" reflection of the uncoated silica splitter. The sampled beam is propagated through an AR-coated, 920-cm, focal-length lens, and folded by three more in-plane reflections off a bare surface BK-7 splitter, and two high-reflectivity mirrors. A minimum of several joules of 1 ω light were required for high-resolution near-field imaging onto film in the original 1 ω diagnostics design. This design necessitated the incorporation of a vacuum cell at the transport focus. The vacuum cell was designed with a tilted, wedged input window to protect the folding mirrors and to eliminate fringing, and had a collimating lens at its output. It was extremely important to have a well-collimated, representative sample of the beam for the wavefront correction system (Hartmann sensor) and for the 1 ω far-field camera. To accomplish this, all flat optics leading to the collimating lens were mounted and interferometrically tested prior to installation. Mounting problems were corrected on several of the large splitters, which allowed us to achieve low-aberration transport to the diagnostic table.

The diagnostics transport enclosure contains the output 1 ω calorimeter as shown in Fig. 4, after three uncoated reflections to keep the calorimeter energy below 1 J. Calculating the Fresnel reflection from all three surfaces determines the transmission coefficient from the main beamline to the calorimeter.

Measurements were made to confirm these values. We changed the 12° angle of incidence for the large splitters to 12.2° due to a 14-cm shift of the 61-cm splitter midway through the frequency converter activation. This mitigated a collimated ghost reflection from the frequency converting crystals, which was reflected and focused by the spatial filter lens onto the splitter, causing damage. The increased angle changed the calculated transmission value by 0.4%. All the splitters were wedged to keep unwanted direct backside reflections and double bounce reflections from the three large splitters outside of the calorimeter aperture. The final uncoated splitter had a 2° wedge and a 0.1% AR coating on the backside, with the estimated overlap between the AR surface reflection and the calorimeter aperture of $<25\%$. The additional energy due to the reflection is $<0.7\%$. No unwanted energy from any of the other splitters fell within the calorimeter aperture.

Figure 5 shows the 1ω diagnostics that are located in a separate enclosure from the diagnostics transport optics to prevent scattered light from entering any of the sensitive diagnostics. After the beam enters the table, 10% of the beam is split off and directed to the wavefront control Hartmann sensor (located on the lower part of Fig. 5), and relayed to the Hartmann lenslet array and

camera. The rest of the beam passes through a path-compensating splitter, a 50% splitter, and a 1:1 vacuum relay. Several pointing and centering mirrors direct the beam from the 50% splitter to the 1ω far-field camera. Due to pointing problems, it was difficult to implement the far-field camera and it was also difficult to obtain attenuating filters with good optical quality. Most of the optical filters could be placed directly in front of the far-field camera, but enough attenuation had to be placed in the near-field filters to prevent damage to those in the far field. We selected Schott KG glass filters placed in front of the focusing lens, filters which could be checked for wavefront quality at 633 nm, yet are optically dense at $1.053\ \mu\text{m}$. These are the same filter types as used in the Hartmann sensor.

The far-field camera was used for some time at $f/100$, but was changed to the rattle pair configuration [Fig. 6(a)]. The rattle pair, based on a photographic film design originally prepared for Nova,² was adapted for use with the Beamlet high-resolution CCD cameras. The Beamlet design uses two pairs of wedged mirrors to create an array of far-field spots variable in both intensity and focus at the camera image plane [Fig. 6(b)]. The first pair of mirrors on the left side are 3-in.-diam partially (50%) reflecting mirrors, tilted to generate an array of

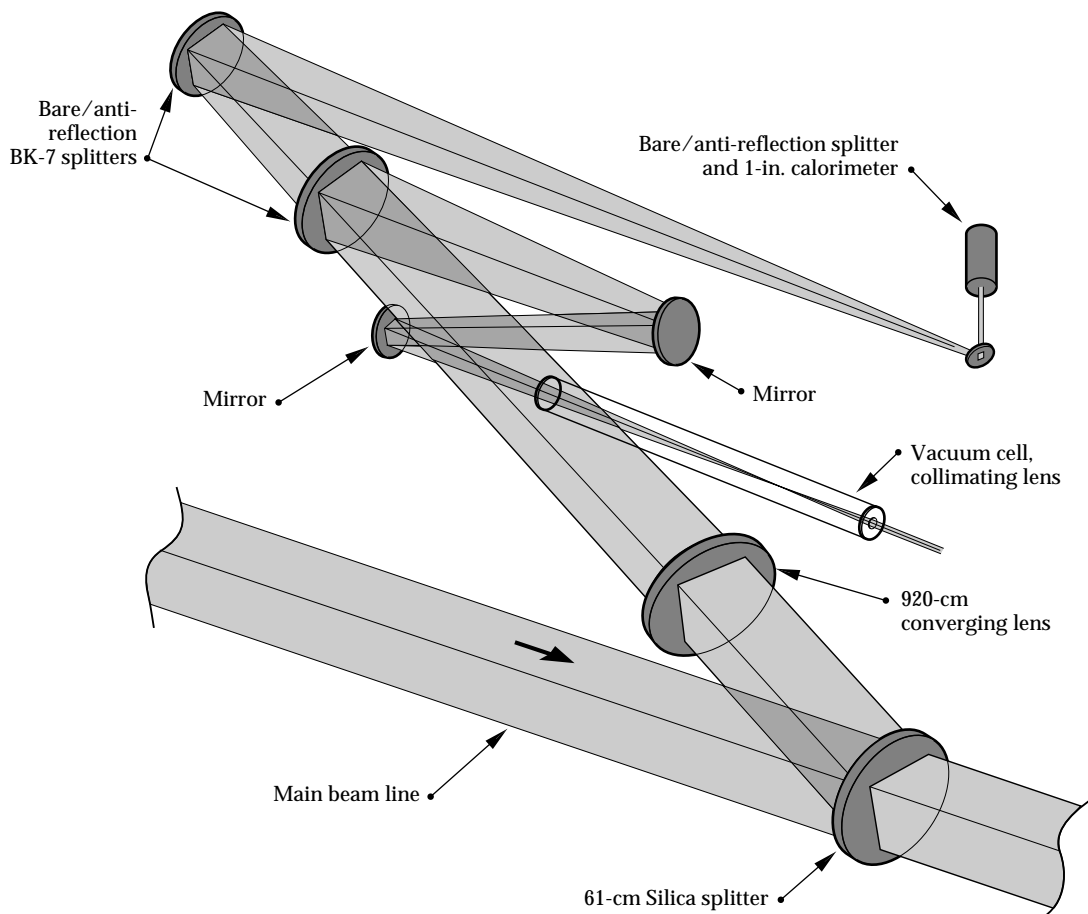


FIGURE 4. The main beam is relayed to the 1ω output diagnostics through a series of uncoated and high-reflector flat optics and is focused by a 9.2-m focal length lens. Up to 10 J is sent through focus in the vacuum cell and collimated. The system 1ω output calorimeter operates directly from three uncoated reflections. (70-50-0494-1682pb01)

spots at the image plane graded in intensity. The focusing lens has a focal length of 1800 mm and is followed by two more wedged mirrors, which have a 90% reflection from their facing surfaces. This second pair of reflectors acts to offset the focus in both angle and longitudinal dimension to take images of the far field through several focal planes. The spacing of the focal planes is adjusted by the spacing between the second pair of mirrors. All rattle pair elements were wedged by 2.4 mrad to mitigate the ghost images from the AR-coated transmission surfaces and were mounted in precision mirror mounts to facilitate system setup. The reflected wavefront quality is important since the beam is reflected numerous times from the same surfaces. To help maintain the wavefront quality, the beam size was kept small on the mirrors (18 mm square), and the mirror reflected wavefront was specified to $\lambda/11$ at $1.05\ \mu\text{m}$, with a gradient $<\lambda/24/\text{cm}$. Excellent results were obtained from this system as described in “System Description and Initial Performance Results for Beamlet,” p. 11. Using the rattle pair camera, we diagnosed dynamic focal plane shifts during a shot. This was a significant aid in correctly applying wavefront pre correction for dynamic aberrations using the Beamlet Adaptive Optics System.

After the main beam passes through the 1:1 vacuum relay (Fig. 5), the recollimated beam is folded twice and directed back through a holographic beamsplitter (HBS)—designed to transmit most of the beam, while diffracting a small amount to either side for diagnostic purposes. The units transmit 10% of the beam energy

into the first order, 1% into the second, etc. This approach was chosen because multiple splitters would have steered the beam and caused unwanted reflections. Initial alignment was difficult, but the HBS performed well for all of the Beamlet activation sequence. Figure 5 shows a first-order beam from the first HBS directed to a vacuum photodiode temporal diagnostic. The photodiode signal is recorded by a Tektronix SCD-5000 transient digitizer for a combined rise time of 110 ps. In addition, the leakage through the second turning mirror, just ahead of the first holographic beamsplitter, is routed out of the diagnostics enclosure to a streak camera for higher-resolution temporal diagnosis. The zero order from the first splitter, which constitutes nearly 78% of the incident beam, is reflected off of a 97% splitter to the radial-shear interferometer and the Fabry–Perot bandwidth diagnostics. Originally, the near-field film camera for high-resolution imaging was to be at this location, but the performance obtained from the high-resolution CCD camera made the film camera unnecessary. The 14-bit dynamic range, 1024×1024 pixel, cooled scientific-grade CCD camera is over 10^6 more sensitive than film and has none of the inherent problems or delays associated with film densitometry. The remainder of the zero-order beam after the 97% splitter is passed through an AR-coated compensating splitter to the second HBS element. The zero order from the second element is relayed into the high-resolution near-field CCD camera, and a first-order beam is relayed to a standard-resolution near-field camera.

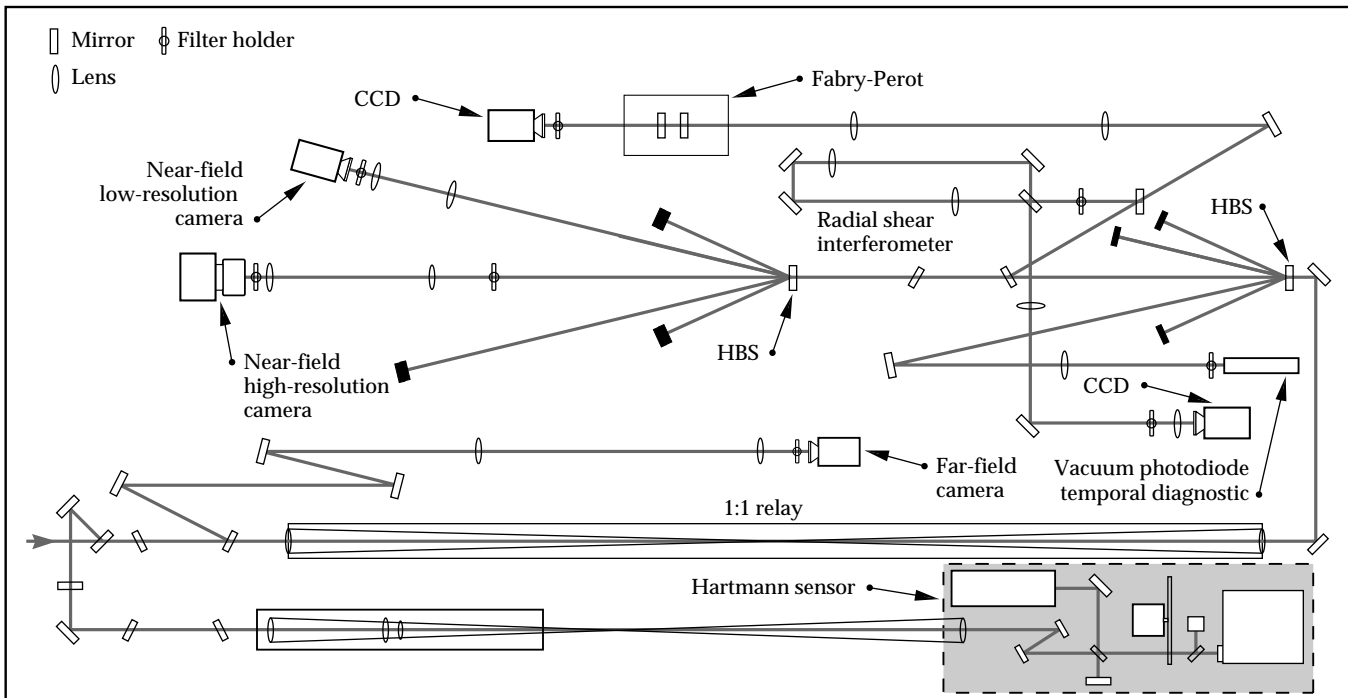


FIGURE 5. Beamlet 1ω output diagnostics include near- and far-field imaging, temporal pulse shape, wavefront, and beam bandwidth. The wavefront control system output sensor (Hartmann sensor) is also located on this table. (See Fig. 4 for the 1ω energy measurement.) (70-50-0395-0666pb01)

2 ω /3 ω Output Diagnostics

The 2 ω /3 ω diagnostic transport optics demagnify and relay all three wavelengths to the specific diagnostics as shown in Figs. 7 and 8. The transport optics use a bare-surface silica splitter identical to the 1 ω splitter, except the back surface has a 3 ω sol-gel AR coating. The splitter is oriented with a 25° angle of incidence, “P” polarized, with the diagnostic beam directed through a 900-cm focal length (at 1 ω) Beamlet spatial filter lens. The converging beam is passed through a 40-cm wedged silica splitter (the calorimeter splitter) with the uncoated front surface reflection sent to the energy balance calorimetry station (described below). The beam transmitted through the calorimeter splitter, which is AR coated on the back side with a compromise 2 ω /3 ω coating, is reflected in plane by a combination bare surface silica splitter and a 1 ω /3 ω high reflector in the lower vertical fold location. The converging 1 ω /2 ω /3 ω beams are then sent through the 3 ω splitter, with a sample of the beams split off by the uncoated front surface, folded by 1 ω /3 ω high reflectors, and sent to the 3 ω diagnostics. The beams are similarly folded to the 2 ω diagnostics with that splitter being a high reflector at 2 ω , and the folding mirrors being at least 95% reflective at both 1 ω and 2 ω to relay the 1 ω alignment beam to the 2 ω diagnostics. The remaining beam, transmitted through the 2 ω splitter, is relayed to a Cohu CCD camera and is used for system alignment.

The 3 ω beam was thoroughly diagnosed, with two near-field cameras, a far-field camera, a vacuum photodiode temporal diagnostic, and a streak camera temporal diagnostic. The energies were measured in the energy balance diagnostic station. The 2 ω beam near-field profile was also diagnosed on a regular basis. Schott filters [UG-5, KG-10, and VG-11 (a nonfluorescing filter glass

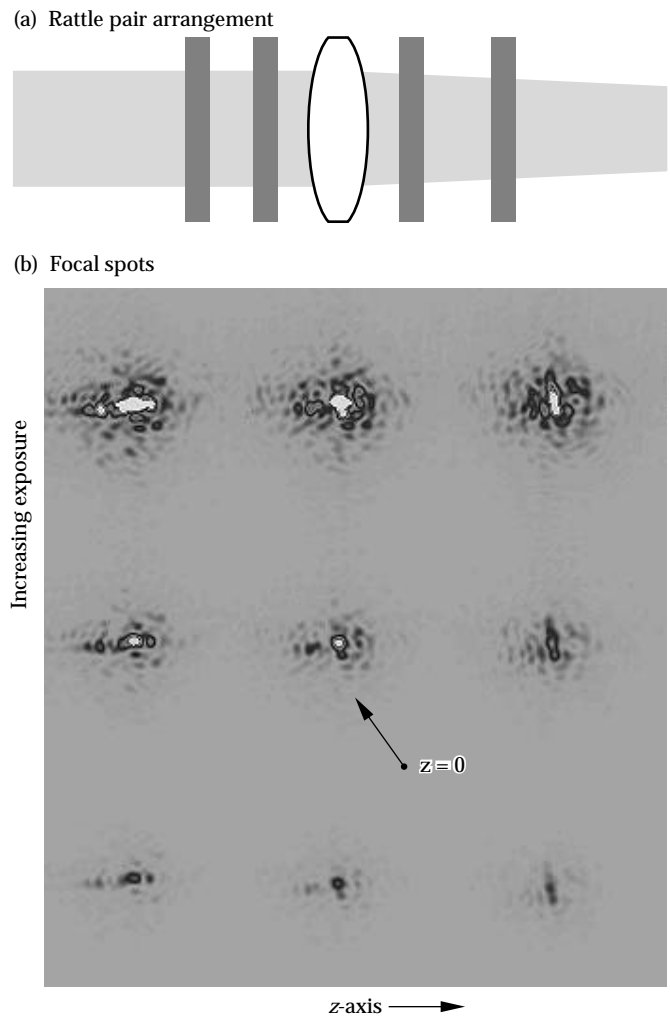
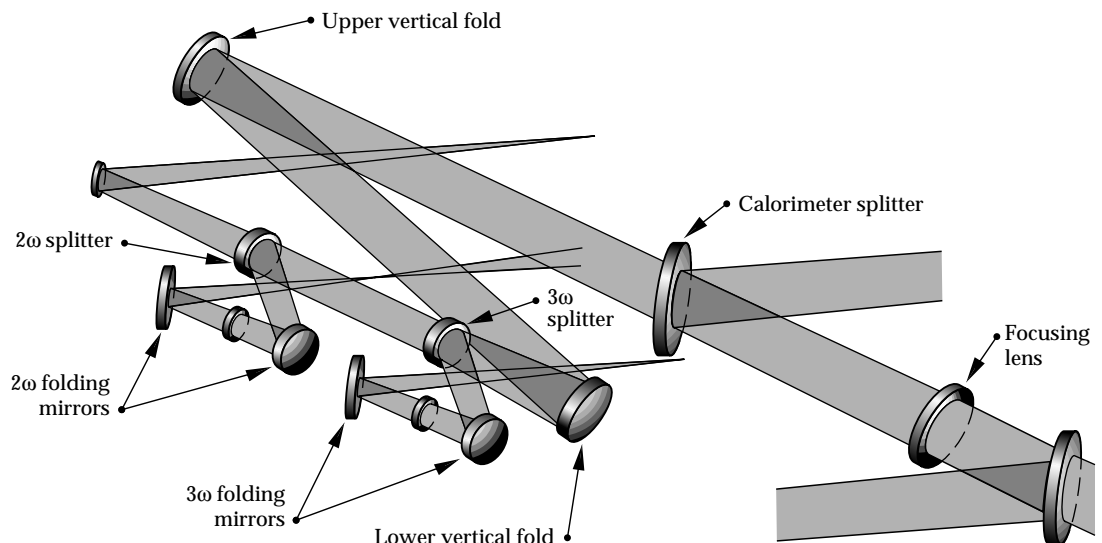


FIGURE 6. Two mirrors arranged as “rattle pairs” and a focusing lens (a) project an array of focal spots onto the high-resolution CCD camera. These focal spots (b) are graded by intensity in one dimension and are different focal planes in the other dimension. (70-50-0395-0667pb01)

FIGURE 7. The doubled and tripled beam is focused and folded using uncoated and dichroic reflectors, and collimated after focus. The 1 ω light is transported to all locations for alignment purposes. A vacuum cell is not required, as the beams are attenuated sufficiently before focus. (70-50-0395-0668pb01)



for blocking 3ω] were used to perform color separation of each diagnostic. We set the energy levels at each diagnostic using attenuating mirrors located just beyond the folding mirrors and by manually inserting neutral density filters.

The $2\omega/3\omega$ diagnostics station transport optics use the 1ω alignment beam to perform pointing and centering for 2ω and 3ω diagnostic paths. We employed dichroic transport mirrors to transmit sufficient 1ω light intensity, an achromatic relay system, and a manually insertable collimation lens (Fig. 8). The design worked well for alignment, but did not determine the near-field camera image planes. The depth of focus at the aperture size of the Cohu 6400 series camera is very small, so calculated locations could not be practically used. A temporary alignment beam, a tripled Nd:YAG, injected into the output spatial filter solved this problem. We located the tripler array image plane on each camera at its design wavelength. Another complication was that the pointing for the three wavelengths was slightly different after passing through the wedged optics, including the large calorimeter splitter. For high angular resolution far-field imaging, we offset the alignment focal spot so that the shot focus would fall within the camera's field of view.

Energy Balance Diagnostics

An accurate energy balance is extremely important to understanding Beamlet operation. A good measure of the absolute energy in each of the three wavelengths, following frequency conversion, impacts decisions and conclusions on frequency converting crystal orientation, 1ω beam divergence, conversion efficiency, and a host

of other laser and frequency conversion parameters. Figure 9 shows the energy balance calorimetry station. The beam from the main $2\omega/3\omega$ uncoated silica splitter is directed to the dispersing prisms after passing through the focusing lens and reflecting from the uncoated silica calorimeter splitter. We used two uncoated silica prisms, each with a 40° apex angle, to achieve a total deviation of 38.9° , 39.9° , and 41.4° for the $1\omega/2\omega/3\omega$ beams, respectively. We use two prisms instead of one because of the thickness limitations of commercially available silica blanks. The pair of prisms are located at a distance

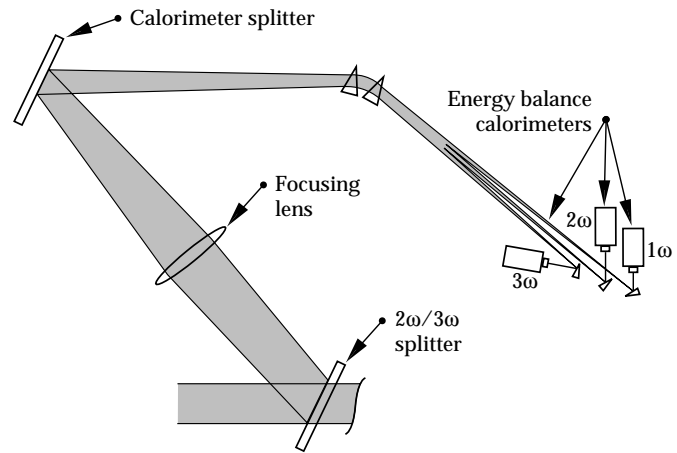


FIGURE 9. The Beamlet energy balance diagnostic relies solely upon uncoated surface reflections to attenuate the beam below 1 J into the calorimeters. Chromatic dispersion is accomplished with two 40° uncoated fused silica prisms, with the total path attenuation calculated from the measured beam incident angles. The sum of the calorimeter energies is routinely within $\pm 2\%$ of the 1ω output calorimeter. (70-50-0395-0670pb01)

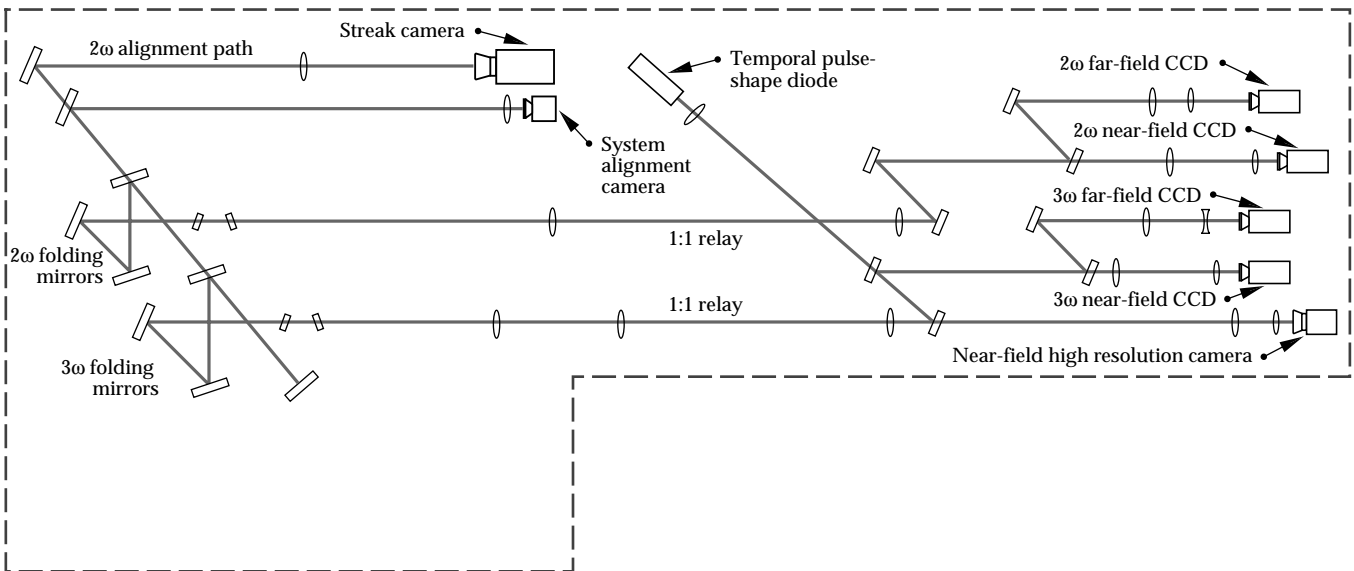


FIGURE 8. Beamlet 3ω diagnostics consist of near- and far-field imaging and temporal pulse-shaping, as well as housing the system alignment camera. (70-50-0395-0669pb01)

from the focusing lens where the beam size allows them to be reasonably small, yet far enough from the calorimeters such that the beams become sufficiently separated. The prisms are mounted on rotation stages with 1 min of resolution, and are aligned to a 30° angle of incidence from the input beam. The dispersed, converging beams are then propagated to a series of uncoated silica 20° wedges that direct the beams into a calorimeter for each of the three wavelengths. We chose the final wedges to ensure that only the first surface reflection would be reflected into the calorimeter.

Altogether, the converging beams undergo three uncoated reflections and are attenuated by about 2×10^{-5} to avoid the possibility of damage to the calorimeter absorbing surface. Using the 1 ω alignment beam, all three calorimeters were aligned by rotating the dispersive prisms by a prescribed amount to deviate the 1 ω beam along the 2 ω path or 3 ω path, respectively. The distance used from the main focusing lens is a calculated value. We used exposed polaroid film in a plastic cover taped over the calorimeter input apertures to confirm the beam size and alignment on a shot. The beam size and locations were exactly what we specified. On the system shots, the sum of the energy balance calorimeters and the other two output calorimeters agreed to well within $\pm 5\%$ (described in the calorimetry section).

Beam-Dump Calorimetry

Figure 10 shows the beam-dump calorimeter—the final diagnostic on the Beamlet beam that absorbs all the remaining 1 ω , 2 ω , and 3 ω light. After the main Beamlet beam goes through the 2 ω /3 ω splitter, it passes through a silica beam expander lens and on to the beam-dump calorimeter. The unit has a 74-cm square aperture, and uses Schott NG-4 glass to absorb all three wavelengths without being damaged by the maximum fluence of any of the wavelengths during the various phases of Beamlet operation.

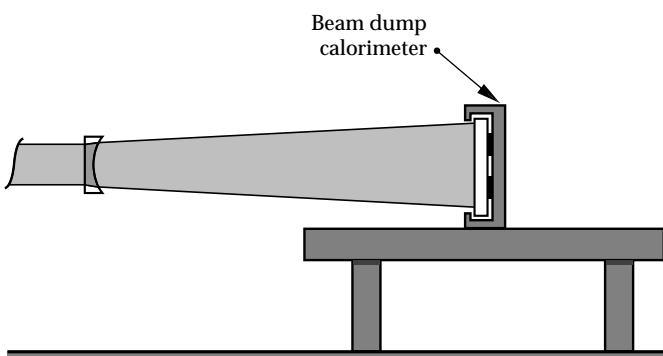


FIGURE 10. Diverging silica lens directs the remaining 1 ω /2 ω /3 ω beam onto the absorbing glass of the beam-dump calorimeter. It is a 74 × 74 cm² design capable of absorbing and diagnosing the full Beamlet output energy at any combination of wavelengths. (70-50-0395-0671pb01)

Calorimetry and Imaging Components

The following sections describe the design, calibration, and performance of the calorimeter components and the imaging components, respectively.

Calorimetry

All of the absolute energy diagnostics on Beamlet consist of absorbing glass calorimeters. A temperature change, due to absorbed laser energy, is measured by thermocouples and is read out by precision nanovoltmeters at a 2-Hz rate. To avoid relying on one model or algorithm, we used three different calorimeter models to measure absolute energy output: (1) The Scientech model 38-0111 (a surplus from Nova) obtained from the Optical Sciences Laboratory; (2) the Scientech model 38-0101 with NG-1 and NG-4 glass to use at all three wavelengths after the frequency converters; and (3) the beam dump calorimeter to absorb the full Beamlet output at all three wavelengths, installed in the main beamline following the fused silica expansion lens.

1 ω Output Calorimeter

The calorimeters in the cavity diagnostics and the 1 ω output diagnostic stations are 1-in.-aperture Scientech model 38-0111 that have a 1/ e decay time of 160 s. The voltage from these devices is of the order of a few to several hundred microvolts, with a sample voltage waveform shown in Fig. 11. To determine the incident energy, the step voltage as determined by the difference between two linear fits (see Fig. 11) was multiplied by an experimentally determined calibration factor. The preshot baseline fit was performed over a

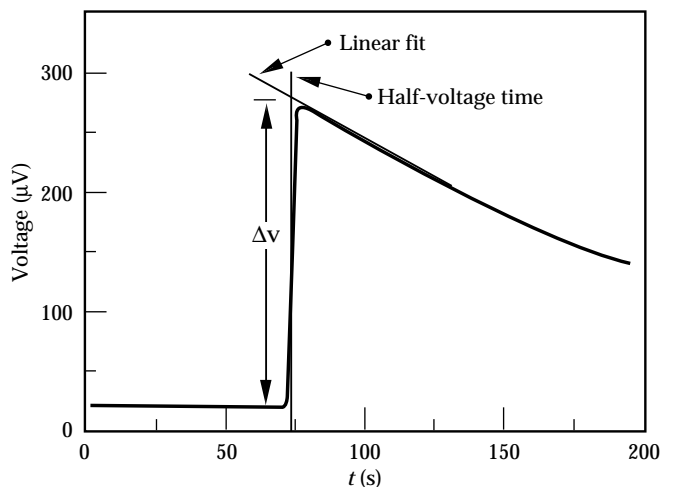


FIGURE 11. Calorimeter waveform for an 8.85-kJ shot. The voltage step is determined between two least-square line fits before and after shot time. The voltage difference is calculated when the rising edge is at the 50% level. Shot energy is then inferred from the calorimeter calibration and optical transport attenuation. (70-50-0395-0672pb01)

60-s interval prior to shot time, and the post-shot fit over a 90-s interval starting 7 s after the shot. This gave the energy on the calorimeter, and the energy in the main beam was inferred from the calculated and measured transmission coefficients of the transport optics.

We used two methods to calibrate the model 38-0111 calorimeter: (1) Using the electronic heater in the calorimeter head for electronic calibration, and (2) by comparison to an optical calorimeter transfer standard from the National Institute of Standards and Technology (NIST). To perform the electronic calibration, we measured the internal heater resistance using the 4-wire technique, then injected a known current over a precise time interval. The amount of injected energy was simply

$$E = I^2 R \Delta t, \quad (1)$$

where I is the injected current, R is the heater resistance, and Δt is the current pulse width. The voltage waveform was captured in the voltmeter measurement buffer (512 measurements long) and analyzed using the Macintosh/LabVIEW systems. The analysis program automatically finds the shot time by searching for the step change and calculating the preshot and post-shot linear fits using predetermined intervals prior to, and after, shot time. Voltmeter resolution was 100 nV, which corresponded to approximately 150- μ J energy resolution. After compensation for the Fresnel loss of the calorimeter's uncoated NG-1 absorber, we calculated an equivalent optical calibration factor K in microvolts/joule.

To perform optical calibration we reflected a short pulse from a Nd:YAG laser off an approximately 50% transmission beam-splitter onto the NIST transfer standard calorimeter and transmitted the remaining 50% of the beam to the calorimeter under test. The fraction of energy split to each of the calorimeters is given by

$$E_{\text{ref}} = \beta E \quad (2)$$

and

$$E_{\text{cal}} = \alpha E = K V \quad (3)$$

where α and β are unknown, E_{ref} is the energy incident upon the NIST calorimeter, E_{cal} is the energy incident

upon the calorimeter under test, K is the undetermined calibration factor, and V is the voltage step for a particular shot. Manipulating these equations, a constant C_1 can be defined as

$$C_1 = K \frac{\beta}{\alpha} = \frac{E_{\text{ref}}}{V}. \quad (4)$$

A series of measurements of E_{ref}/V determined C_1 . Then, the NIST calorimeter and the calorimeter under test were exchanged such that the NIST calorimeter was on the αE split and the calorimeter under test was installed in the βE split. Another series of measurements of E_{ref}/V determined constant C_2 , which was similarly defined as

$$C_2 = K \frac{\alpha}{\beta} = \frac{E_{\text{ref}}}{V}. \quad (5)$$

The calibration constant for the calorimeter under test was then determined from

$$E = I^2 R \Delta t, \quad (6)$$

Note that this calibration technique is entirely independent of the shot-to-shot repeatability of the laser source, does not require knowledge of the splitter ratio, and does not require that the splitter and transport paths be lossless ($\alpha + \beta$ does not have to equal 1). The optical and electrical calibrations are in excellent agreement between the two techniques ($\pm 1.5\%$).

Energy Balance Calorimeters

The Energy Balance Calorimetry station uses the 1-in. Scientech model 38-0101. It has a $1/\epsilon$ time constant of 16 s, which is too fast to use the linear extrapolation method previously described. For these calorimeters, the main problem with backward linear extrapolation is the extreme sensitivity to shot time determination. Therefore, we used an alternative method, where we integrate the area under the curve—the volt-seconds of the voltage waveform. As before, we use an edge-detection algorithm to find shot time and then integrate over a 70-s interval starting at shot time (the same used for calibration). An issue with these calorimeters is the baseline drift, due to temperature fluctuations within the laser bay, similar to the slower model 38-0111 calorimeters. The baseline drift is quantified using an algorithm to interpolate between the baseline value

measured before and after the laser shot. The incident energy is then calculated from the total integrated calorimeter signal voltage (minus the correction for baseline), and the integrated signal is related to the laser energy using a calibration constant.

Because of the excellent agreement between electrical and optical calibration demonstrated on the model 38-0111 calorimeters, only electrical calibration was performed on the model 38-0101 calorimeters. While the electrical calibration values were not as repeatable as the slow-decay-time model 38-0111 calorimeters, they still provided results well within the requirements for the Beamlet diagnostics.

Beam-Dump Calorimeter

The beam-dump calorimeter, designed and fabricated using Nova's 74-cm calorimeter as a guide, absorbs the full Beamlet energy at all three wavelengths. The main absorbing element is a 76-cm-square, 0.25-in.-thick Al plate, tiled with 4-mm-thick, 6-in.-square panes of NG-4 absorbing glass. The glass thickness was selected to attenuate incident 1ω energy to $<25 \text{ mJ/cm}^2$, which is 10% of the level at which damage to the glue holding the absorbing glass has been known to occur. For this reason, we chose 4-mm-thick NG-4, which is just sufficient for full energy 1ω shots, yet has enough absorption depth at 2ω and 3ω full-energy shots to avoid surface damage. The sensing elements are type K thermocouples glued in a 7×7 array on the back side of the Al plate, wired to reference thermocouples attached to a dummy plate located in the back of the calorimeter body. The thermocouples are standard types from Omega, and are glued to the Al using a high-thermal-conductivity epoxy and are electrically wired in series using similar-metal terminal blocks. The only unwanted thermocouple junctions are where the output connector copper wires connect to the first and last thermocouple leads on one of the terminal blocks. Those connections are adjacent to minimize temperature differences. The entire absorbing plate assembly is mounted using insulating spacers to a support structure, designed to provide protection from air currents.

We use NIST traceable standards and a high-power laser to perform full-scale optical calibration in the Nova calorimeter calibration facility. To achieve reasonable signal levels, approximately 500 J in 1 s was directed onto the calorimeter in a round beam (unlike the square Beamlet beam). This was sufficient to obtain about $70 \mu\text{V}$ for calibration, and resulted in a calibration factor of $0.1417 \mu\text{V/J}$. This calibration factor was about 2% higher than that determined using standard Nova waveform analysis methods, a difference due to how the voltage waveforms are interpreted. In Nova, the voltage step is calculated by the difference between the peak of the voltage waveform and the extrapolated baseline. For Beamlet, the voltage step is calculated by the difference

between the linear least-square fit of the baseline before the shot, and the linear fit of a waveform segment after the shot. This difference is calculated at the time when the voltage waveform is half of its peak value. The Beamlet analysis technique has the advantage of averaging many measurements during the voltage waveform decay.

Calorimeter Performance

The performance of the calorimeter system was repeatable to better than $\pm 2\%$ for the model 38-0101 calorimeters and approached $\pm 1\%$ for the model 38-0111 calorimeters during calibration. To test this, we compared their performance during system operation using calculated and measured transmission values to propagate the energy results back to "standard" beam-line locations. Comparison between the 1ω output calorimeter and the energy balance calorimeters was done at the first surface of the $2\omega/3\omega$ calorimeter splitter. Comparison between the energy balance calorimeters and the beam dump calorimeter was made at the surface of the beam dump calorimeter.

Figure 12 compares the calorimeters for a series of shots taken in August and September, 1994. We met our original specification for the Beamlet calorimetry system, which was to achieve better than $\pm 5\%$ absolute accuracy. The most remarkable observation about the agreement is that three totally independent calorimeter systems, two separate analysis algorithms, and three separate calibration systems were used to achieve this level of accuracy. Because of this agreement, the Beamlet project scientists can report on laser and frequency converter performance with a high degree of confidence.

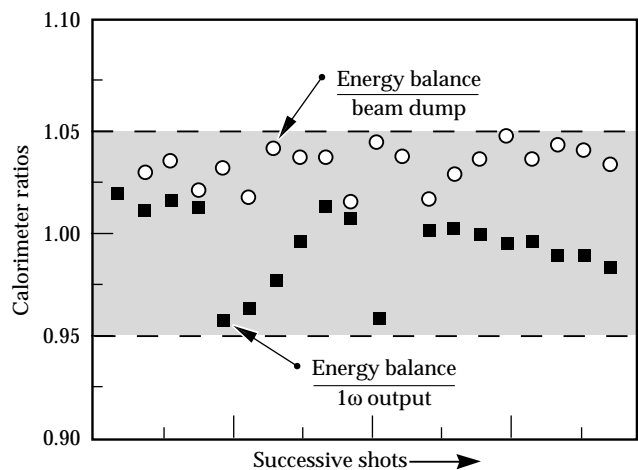


FIGURE 12. Comparison between the three output calorimeter systems for a sequential series of Beamlet shots in August and September 1994. Shown are the ratios of the measured energies between the 1ω output calorimeter, sum of the energy balance calorimeters, and the beam-dump calorimeter. In all cases, the sum of the energy balance calorimeters agrees with the other two systems to better than 5%. (70-50-0395-0673pb01)

Imaging Diagnostics

Imaging of the laser beam is done extensively on Beamlet. This is of great importance for diagnosing the beam during the four passes in the main cavity and out through the booster amplifier. In the cavity diagnostics, near-field imaging of the beam at the cavity mirrors is useful for preshot beam centering, for measuring the spatial beam profile in the various passes, and for measuring the extinction of the plasma-electrode Pockels cell during the fourth pass. In the output 1ω diagnostics, the near-field image at the frequency converter crystals is vital for ensuring that the beam intensity profile converts efficiently and that damaging intensity modulation is not present in the beam. Imaging of the beam at focus is also done in the 1ω output diagnostics to understand the quality of the beam phase-front before conversion. After frequency conversion, both near-field and far-field images of the beam at 2ω and 3ω are taken, and prove to be very useful to understanding the performance of the laser system and the frequency converter crystals. All of the images use CCD cameras/framegrabbers or dedicated high-resolution scientific-grade CCD cameras.

The standard-resolution cameras we use in all the diagnostic packages are Cohu 6400 remote head CCD cameras, which have a $6.4 \times 4.8 \text{ mm}^2$ active area, and have 739 wide \times 484 high picture elements. The model 6400 is a frame transfer camera, where the charge storage cell is shared between adjacent horizontal lines. Because of this, only 242 horizontal lines have shot data available for analysis from the framegrabber system. We investigated the use of the interline transfer camera, which is a microlensed CCD chip incorporated into certain models of Cohu and Pulnix cameras. The camera can be configured to integrate over $1/30 \text{ s}$ and has the complete image frame in consecutive field transfers that can be merged in software. Another camera type from Cohu, which has a frame transfer CCD chip with dual charge storage cells, also outputs two consecutive fields (a full frame) with image data from a shot. However, it would have required development work by the manufacturer of the framegrabber/analysis system. We therefore stayed with the standard system that produces images with a spatial resolution of 240×240 pixels, digitized 8 bits deep (identical to the Nova framegrabbing system). Higher spatial resolution is somewhat of a liability because of the increased storage space requirements and slower image analysis.

We perform high-resolution imaging using a Macintosh-controlled scientific-grade CCD camera. The camera has 1024×1024 pixels digitized 14 bits deep, and is Peltier cooled to -55°C for low noise integration and readout. It is especially useful in replacing the original film-based camera systems in the 1ω diagnostics, because film has poor sensitivity at $1.054 \mu\text{m}$. An additional advantage of the high-resolution

camera is that the results are immediately available for analysis. It was also used for high-resolution surveys of Beamlet using the alignment beam, where the high dynamic range proved extremely valuable. Because of our positive experience with these cameras, we purchased an additional camera, 512×512 pixels, which has a full 16-bit dynamic range.

Data Acquisition System

The Beamlet data acquisition system consists of a SUN Sparc Station operating LabVIEW software to control all the laser diagnostics. There are six types of diagnostic devices interfaced to this system: the Tektronix TDS-320 oscilloscope and SCD-5000 transient digitizer, HP 34401A and HP 3478A voltmeters, IO-Tech digital IO box, and Kiethley 220 current source. The streak camera and high-resolution camera are operated in standalone mode, although the streak camera is initiated by the system trigger, and the high-resolution camera uses a software trigger through the IO-Tech box over the GPIB network.

The National Instruments LabVIEW control system is used to provide setup, control, data acquisition, and analysis. Before a shot, each diagnostic has to be specifically activated and in some cases software-triggered. After everything is set up, the diagnostics operator selects a particular menu item to inform shot control that the diagnostics are configured and ready for the shot. Upon initiation of the main capacitor bank charge, the diagnostics control software interprets the shot state and takes background data on all the calorimeter channels; the shot either occurs before the voltmeters run out of buffer space or else is aborted. Following the shot, the acquisition system pauses until the calorimeter voltmeters have completed acquisition and then polls the diagnostics for data. The system acquires all the data from the remote devices, stores it to disk, then retrieves it for analysis. Thus if there is a storage problem, it is discovered immediately and steps can be taken to retrieve the data again from the instruments. Data analysis is limited to basic waveform analysis of the energy diagnostics, calculation of the round-trip cavity system gain, and display of the oscilloscope traces.

Imaging diagnostics, other than the high-resolution camera, is operated by the Coherent Big-Sky system,⁴ which performs framegrabbing on 16 channels, simultaneously. All of the cameras in the diagnostics system are routed to the 30×30 video switcher, which supplies the video signals to the Big-Sky system. The Big-Sky system receives a system trigger to select which frame to grab. After the shot, the diagnostic operator manually saves the results on the Big-Sky computer and transfers the video files to the SUN system for storage and archiving.

Summary

We developed a comprehensive set of diagnostics for the Beamlet laser system to provide all of the information necessary for determining the laser performance. Optical transport systems for demagnifying laser beam samples in four separate diagnostics stations demonstrate low-aberration performance, which is key to obtaining far-field images of the 1ω beam at the output section. The primary energy diagnostics, absorbing glass calorimeters, are installed throughout the system and demonstrate outstanding accuracy and reliability. Calibration repeatability is well within $\pm 1\%$. New acquisition methods, such as using voltmeters to replace the Nova calorimeter amplifiers and analysis techniques adapted from the Optical Sciences Laser, enable us to achieve agreement between multiple calorimeters of much better than $\pm 5\%$. The imaging diagnostics make wide-scale use of CCD cameras, with nearly half the number of installed cameras as the Nova system. Beamlet is also the pioneer in using high spatial-resolution and high dynamic-range, scientific-grade CCD cameras to replace film for beam profiling and far-field imaging. The diagnostics were activated on time and were key to achieving the Beamlet performance goals.

Acknowledgments

We thank the optical engineers D. Aikens, K. Moore, and W. Whistler, who designed and procured the large number and variety of optical elements required by Beamlet diagnostics. We give special thanks to R. Speck for his excellent analysis, where he compared the different system calorimeters and obtained the outstanding results shown in Fig. 12.

Notes and References

1. C. W. Laumann, J. L. Miller, C. E. Thompson, et al., *ICF Quarterly Report* 4(1), 1–9, Lawrence Livermore National Laboratory, Livermore, CA, UCRL-LR-105821-94-1, (1994).
2. P. J. Wegner and M. A. Henesian, Lawrence Livermore National Laboratory, Livermore, CA, UCRL-JC-106786 (1991).
3. LabVIEW data acquisition and control programming language LabVIEW, National Instruments Corp., 6504 Bridge Point Parkway, Austin, TX, 78730-9824.
4. Coherent Big-Sky System, an imaging diagnostics system, Coherent Inc., Instruments Division, 2301 Lindbergh Street, Auburn, CA 95602, (916) 888-5107.